Boundary-Layer Meteorol
DOI 10.1007/s10546-006-9091-3

ORIGINAL PAPER

Interactions of an urban heat island and sea-breeze circulations during winter over the metropolitan area of São Paulo, Brazil

Edmilson D. Freitas · Christopher M. Rozoff · William R. Cotton · Pedro L. Silva Dias

Received: 31 May 2005 / Accepted: 24 April 2006

Abstract The Town Energy Budget (TEB) model, a detailed urban parameterisation using a generalised canyon geometry, coupled with the Regional Atmospheric Modelling System (RAMS) is used to simulate the wintertime local circulation in the megacity environment of the metropolitan area of Sao Paulo (MASP) in Brazil. Model simulations are performed using actual topography and land-use fields. Comparison with a simple urban parameterisation based on the LEAF-2 scheme is also shown. Validation is based on comparison between model simulations and observations. Sensitivity tests with TEB reveal an important interaction between the sea breeze and the MASP heat island circulation. Even though topography is known to play an important role in the MASP region's weather, in these tests the simulations were performed without topography in order to unambiguously identify the interaction between the two local circulations. The urban heat island (UHI) forms a strong convergence zone in the centre of the city and thereby accelerates the sea-breeze front toward the centre of the city. The presence of the urban region increases the sea-breeze front propagation mean speed by about $0.32\,\mathrm{m\,s^{-1}}$ when compared with the situation of no city. After its arrival in the urban region, the sea-breeze front stalls over the centre of the city for about 2 h. Subsequently, the sea breeze progresses beyond the city when the heat island dissipates. Thereafter, the sea breeze propagates beyond the urban area at a decelerated rate compared to a simulation without an UHI.

Keywords RAMS · Sea breeze · Surface scheme · Urban heat island

E. D. Freitas (✉) · P. L. Silva Dias
Departamento de Ciências Atmosféricas, Instituto de Astronomia,
Geofísica e Ciências Atmosféricas, Universidade de São Paulo,
Rua do Matão, 1226,
CEP 05508-090, São Paulo, S.P., Brazil
e-mail: efreitas@model.iag.usp.br

C. M. Rozoff · W. R. Cotton
Department of Atmospheric Science, Colorado State University,
Fort Collins,
Colorado, USA, 80523

1 Introduction

Recently, there has been increased interest in the modification of atmospheric circulations by surface heterogeneities. The urban surface, in particular, affects sensible heat, latent heat and momentum fluxes, surface convergence, boundary-layer height, and other boundary-layer features. Such changes impact upon pollution dispersion, thunderstorm initiation, optical properties of the atmosphere, and many other physical and chemical processes in the urban environment (e.g., observational results from Changnon et al. 1971; Oke 1978; Balling et al. 1990; Morris et al. 2001; Dixon and Mote 2003; and modelling results from Sailor 1995; Khan and Simpson 2001).

During the winter in urban areas, with the low availability of solar energy, pollutant concentrations can be very critical since the development of the planetary boundary layer (PBL) is limited. In this case, pollution dispersion is highly dependent on the strength of the heat island circulation (HIC) i.e., the local circulation generated by the thermal contrasts associated with the heat island, and on the synoptic-scale winds. Such winds are known to influence the HIC (Bornstein 1975; Kimura 1976). Under calm conditions the development of the HIC is stronger. Modelling results show that under strong large-scale background winds the HIC is weakened due to the efficient vertical mixing of the air, and the urban heat island (UHI) effect is concentrated closer to the surface (Baik et al. 2001). Kim and Baik (2002), using 24 years of observations made at two meteorological observatories, also verified that the average maximum UHI intensity is weaker in summer and stronger in autumn and winter. The maximum UHI intensity, more pronounced in clear sky conditions, occurred more frequently at night than during the day, and decreased with increasing wind speed. In the absence of wind, closed circulations analogous to the sea breeze can form over the city (HIC), and due to these circulations, and the ducting and trapping of air flow inside street canyons (e.g. Stull 1988 and modelling results from Baik and Kim 2002; Kim and Baik 2004), pollutants that are emitted may stay trapped, with resultant high concentration levels. In such cases, transient circulations, such as associated with frontal systems and the sea breeze, represent the primary mechanism for pollution dispersion.

Interactions between the HIC and the sea breeze have frequently been studied, and reported in the recent literature. Using a two-dimensional model, Ado (1992) found that Tokyo's HIC decays under the influence of a moderate wind but persists in the sea-breeze system and has a notable effect on the sea-breeze pattern. Tokyo's UHI affects the sea breeze by forming a suburban stagnation region, increasing the horizontal temperature gradient, and delaying the advance of the sea breeze inland. Also using a numerical model, Yoshikado (1994) suggested that the UHI may persist under the influence of the sea breeze and interact with it. The sea-breeze front has a tendency to remain over the city due to the effect of the HIC, which can cause convergent flow patterns, particularly in cities close to a coast. Another observation of this work is that the interaction between the HIC and the sea breeze is more significant when: (1) larger urban regions are involved; (2) the urban area is sufficiently far from the coast such that the HIC has ample time to develop. Similar results were obtained from the observational study of Yoshikado and Tsuchida (1996) and modelling results from Ohashi and Kida (2002), which show that sea-breeze and heat-island coupling prevents further inland movement of the sea breeze. Because of a persistent convergence zone over the urban area, significantly high concentrations of pollutants result over the city. Following modelling results from Khan and Simpson (2001), the advancement of the sea breeze inland can be accelerated for many hours due to the

urban effect. The sea breeze can also modify the UHI pattern. Gedzelman et al. (2003), studying the UHI of New York with a mesoscale network of weather stations, verified that during spring and summer sea breezes commonly reduce and delay the HIC and displace it about 10 km inland. Thus, there is no complete agreement concerning the impact of the UHI on the propagation speed of the sea-breeze front. Our study addresses this question in more detail in the context of the metropolitan area of São Paulo (MASP).

A significant difficulty in modelling an urban area is adequately representing the complex urban surface and its effects on boundary-layer turbulent heat and momentum fluxes. Frequently, models use the bare soil formulation or make some adjustment in their surface-vegetation-atmosphere transfer (SVAT) scheme parameters. For example, the original SVAT in the Regional Atmospheric Modelling System (RAMS: Walko et al. 2000), neglecting heterogeneous three-dimensional (3D) structure and anthropogenic heat sources, simply parameterises the urban surface through adjustments in its "biophysical" parameters. As pointed out by Masson (2000), such approximations are satisfactory for large temporal or spatial averages, but when smaller scales are considered it is necessary to incorporate a more detailed scheme.

Using two different surface parameterisations, we present simulations for the wintertime in the MASP with the RAMS version 4.3 (Pielke et al. 1992; Cotton et al. 2003). RAMS 4.3 includes significant changes in the model coding structure using Fortran90 features and more efficient parallelisation.

In Section 2, we present data used for the validation of the model and discuss model characteristics. Section 3 gives the methodology used in studying the HIC and sea-breeze interaction. In Section 4, results of the simulations are discussed, and finally, the conclusions are presented in Section 5.

2 Observations and model characteristics

2.1 Observations

Time series of 2-m temperature and relative humidity are used for the validation of the coupling between RAMS and the Town Energy Budget (TEB: Masson 2000). The surface data chosen to validate the model were collected by the State of São Paulo Environmental Protection Agency (CETESB) automatic monitoring network in four locations in the MASP area. An additional conventional meteorological station at the Institute of Astronomy, Geophysics and Atmospheric Science of the University of Sao Paulo (IAG-AF) within MASP was added to the validation. The domain of the two model grids and location of the stations are presented in Fig. 1; also included is an illustration of the region's topography. The comparison period is 2100 LT (Local Time = UTC – 3 h) 31 July 1999 to 2100 LT 3 August 1999. During this period there was an intensive field experiment in the MASP area, designed to explore the impact of meteorological conditions on pollution concentration.

For qualitative comparison, wind profiles were taken from the PA-2 REMTECH Doppler sodar to verify the vertical wind profiles in the model simulations. The Sodar was installed on the top of the Department of Atmospheric Sciences of the University of Sao Paulo (23° 33′ 35″ S; 46° 43′ 55″ W) during the wintertime of 1999 and was operated with a 50-m vertical resolution and a 15-min temporal resolution.

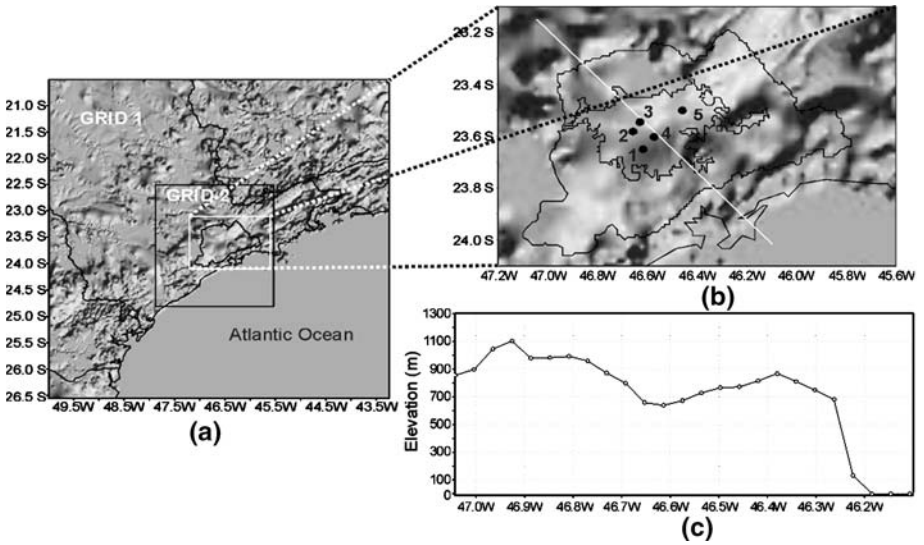

Fig. 1 (**a**) Domain of the two model grids used in this study. In the background is the topography of the region. Contours on the grid 1 are state borders. The contour on the centre of the second grid represents the MASP. (**b**) Zoomed view of the MASP with the inner contour representing its most urbanised region. The numbers indicate the five stations used, as follows: (1) IAG-AF; (2) Ibirapuera; (3) Pq. D. Pedro II; (4) São Caetano do Sul and; (5) São Miguel Paulista. (**c**) Elevation cross-section indicated by the white line in (**b**)

Table 1 Options available in RAMS used during these simulations

Number of points in lateral boundary region used for nudging	5
Nudging time scale at lateral boundary	3600 s
Nudging time scale at the top of domain	10,800 s
Lateral boundary condition	Klemp and Wilhelmson (1978)
Shortwave/Longwave radiation type	Mahrer and Pielke (1977)
Frequency of radiation tendency update	180 s
Number of soil layers	4 (−2.0, −1.5, −0.25 and −0.05 m)
Turbulence parameterisation	Anisotropic deformation (Smagorinsky, 1963) modified based on formulations of Hill (1974) and Lilly (1962)

2.2 Mesoscale model

The model used in this work is the RAMS, which has two interactive nested grids of 16 and 4 km grid spacing for grids 1 and 2, respectively. Grid 1 has 40×40 points covering an area of $624 \times 624\,\text{km}^2$ and grid 2 has 58×62 points covering an area of $228 \times 244\,\text{km}^2$. In the vertical, 28 stretched sigma levels are employed, with grid spacing starting at 70 m and increasing progressively with height at a stretching factor of 1.2 up to a level where 1000 m spacing is attained. All vertical grid spacing above this height are maintained at a constant 1000 m. We note the first model level is located 33.4 m above ground level. Table 1 shows some of the options used in the current model simulations.

Global analyses are obtained from the Brazilian National Centre of Weather and Climate (CPTEC) atmospheric general circulation model (AGCM), whose data originate at 6-h intervals and at grid spacing of $1.875° \times 1.875°$. Temperature, relative humidity, geopotential height, and the horizontal wind components (u and v) are taken from the global analyses for the initial conditions in RAMS. These analysis data are supplemented with surface temperature, surface relative humidity, and surface pressure from the CETESB network.

2.3 Surface parameterisations

In the current study, the first urban parameterisation examined is the original Land Ecosystem-Atmosphere Feedback (LEAF-2) model (Walko et al. 2000), which adapts biophysical parameters, such as the leaf area index, fractional coverage, displacement height, roughness height, albedo, and emissivity, to model the urban portions of grid cells. Within MASP, the predominant land-use land classes (LULCs) are wooded grassland, crop/mixed farming, and urban land. The biophysical parameters corresponding to these LULCs are presented in Table 2. The LEAF-2 parameters were not changed during the simulations.

Closer examination of Table 2 shows that some of the standard parameters used in LEAF-2 are not appropriate for MASP. For example, z_0 and d, which affect momentum fluxes inside the urban canopy and at the first model level, are too small for MASP. Some experimental estimations of roughness length for homogeneously built-up areas were reviewed by Wieringa (1993). For the case of regularly built towns, roughness lengths were found to lie between 0.7 to 1.5 m. In the case of high-rise urban surface ($h > 20$ m), which is the case of central part of MASP, Grimmond and Oke (1999) suggest roughness length values greater than 2.0. As a first approximation, the values of $0.1\,h$ and $0.6\,h$ are usually used for the determination of z_0 and d, respectively.

The second urban parameterisation utilised in our study is the TEB (Masson 2000) model. In TEB, a generalised canyon geometry replaces the usual bare soil formulation or simple one-layer plant canopy often used to represent urban (and suburban) areas. TEB improves the radiation budget as well as the momentum, latent heat, sensible heat, and storage fluxes. As verified by Rozoff et al. (2003), the TEB scheme has a superior performance over LEAF in representing the UHI effects. In addition, TEB provides bulk industrial and vehicular contributions to the sensible and latent heat fluxes. The industrial contribution is roughly constant in time in MASP as pointed out by CETESB (during daytime hours). In contrast, vehicular contributions are much more complex and they must be considered carefully. In addition to a myriad of varieties of vehicles, the number of running vehicles within the city is not constant in time. Incorporating estimates of gasoline and diesel fuel consumption, electricity use,

Table 2 Some of the parameters used in the LEAF model for three different types of LULCs

Parameter Class	Albedo	Emissivity	Leaf area index	Roughness length z_0 (m)	Zero-plane displacement d (m)	Root length (m)
1. Wooded grassland	0.18	0.96	5.0	0.51	3.6	1.0
2. Crop/mixed farming	0.20	0.95	6.0	0.06	0.7	1.0
3. Urban	0.15	0.90	4.8	0.80	1.1	0.8

population data, and the two rush hours per day, Khan and Simpson (2001) developed a complex diurnal cycle of anthropogenic heat fluxes for the city of Brisbane, Australia. A similar approach is used by us, where the diurnal cycle of anthropogenic heat is represented as a superposition of two normal distributions:

$$E(t) = E_{\text{fac}} \left\{ \frac{1}{\sigma_1 \sqrt{2\pi}} \exp \left[\frac{\left(t - \overline{t_1}\right)^2}{2\sigma_1^2} \right] + \frac{1}{\sigma_2 \sqrt{2\pi}} \exp \left[\frac{\left(t - \overline{t_2}\right)^2}{2\sigma_2^2} \right] \right\}, \tag{1}$$

where $E(t)$ is the time dependent contribution from vehicles, E_{fac} is the contribution factor for heat and humidity sources, σ_1 and σ_2 are the standard deviations of each normal distribution, representing the two peak hours of the day, and $\overline{t_1}$ and $\overline{t_2}$ represent the peak hours.

To obtain a more realistic UHI, the MASP is divided into two different LULCs: urban type 1, which predominantly contains high-rise buildings and covers 400 km^2, and urban type 2, which mainly contains residential and industrial regions and covers 1097 km^2. These two regions are defined from LANDSAT-5 imagery and are classified according to the original land-cover categories provided by the International Geosphere-Biosphere Programme (IGBP). Table 3 summarises various key TEB parameters of the two LULCs (based on Tarifa and Azevedo 2001; Khan and Simpson 2001). Non-urban LULCs in the model domain are always parameterised via LEAF-2.

3 Methodology

3.1 Validation of the coupling

For the validation of the coupling, a comparison between simulations using the LEAF-2 and TEB urban formulations is made. Temperature and relative humidity time series from the lowest model level (33.4 m) are used for qualitative validation of the coupled schemes. Time series are obtained from the grid points closest to each station. In addition, Doppler sodar vertical wind profiles are used for qualitative comparison with model data. It is important to note that only a qualitative comparison between sodar and modelled winds is chosen, as the vertical spacing of the data and the area covered by the equipment are different from those in the model.

Table 3 Some differences between the two urban areas used in TEB during this evaluation Based on Tarifa and Azevedo (2001) and Khan and Simpson (2001)

	Urban 1	Urban 2
Building height (m)	50	5
Building width (m)	25	5
z_0(m)	5.0	0.5
Vehicular sensible heat source (W m^{-2})	30 (maximum)	20 (maximum)
Vehicular latent heat source (W m^{-2})	7 (maximum)	5 (maximum)
Industrial sensible heat source (W m^{-2})	20 (constant)	30 (constant)
Industrial latent heat source (W m^{-2})	40 (constant)	50 (constant)

Statistical tests allow quantitative evaluation of TEB's performance in MASP. One useful method involves calculating correlation coefficients between simulated and observed variables for each station. Pearson's linear correlation (see, for example, Wilks 1995), given by the ratio between the covariance of two variables and the product of their standard deviations, provides such correlation coefficients.

Although correlation coefficients evaluate the linear relationship between simulated and observed variables, such an analysis fails to account for bias. Therefore, a useful supplemental method is the mean error (ME), given by

$$\mathrm{ME} = \frac{1}{n}\sum_{k=1}^{n}(y_k - o_k) = \overline{y} - \overline{o}, \tag{2}$$

which is an expression for the bias of the simulation. To gauge a simulation's accuracy, the mean square error (MSE) is also computed:

$$\mathrm{MSE} = \frac{1}{n}\sum_{k=1}^{n}(y_k - o_k)^2, \tag{3}$$

where high values of MSE indicate a high level of discrepancy between simulations and observations. The root square of MSE (RMSE) represents the typical magnitude of the simulation error and it has the same dimension as the original variable. Pielke (2002) presents another parameter, $\mathrm{RMSE_{UB}}$, to evaluate the skill of a simulation:

$$\mathrm{RMSE_{UB}} = \left\{\frac{1}{n}\sum_{k=1}^{n}\left[(y_k - \overline{y}) - (o_k - \overline{o})\right]^2\right\}^{1/2}, \tag{4}$$

which represents the unbiased root MSE after a mean deviation is removed.

3.2 Interactions between the UHI and sea breeze

Using TEB in RAMS, two simulations are carried out to understand the interactions between the HIC and sea breeze. The simulations were initialised with a horizontally homogeneous temperature, relative humidity, and geopotential height vertical profiles obtained from CPTEC AGCM analyses for 0300 LT 1 August 1999 from a point close to the coast. The wind speeds were initialised near zero, and so there is no baroclinicity in the initial condition, which is basically at rest. The two simulations differ in their LULCs; namely, a control simulation imposes the normal LULCs corresponding to MASP, while the other experiment replaces all suburban and urban land use with the average surrounding vegetation in the area. These experiments neglect topography, since only the interactions between the two local circulations are of primary interest. The length of integration is 48 h, the horizontal grid spacing is 4 km, and there are 28 vertical levels configured in the exact manner described earlier.

For convenient visualisation, vertical cross-sections are presented to explore interactions between the HIC and sea breeze. The orientation of the cross-section is perpendicular to the seashore (north-west to south-east orientation; see the white line in Fig. 1a), through the points (46.575° W, 23.559° S), inland, and (46.146° S, 23.955° S) at the coast. The distance between these two points is approximately 62 km. For useful interpretation, the horizontal wind is projected onto this cross-section, hereafter referred to as the sea-breeze wind (U_{sb}).

4 Results

4.1 Results from the validation

Figures 2–6 provide time series for temperature and relative humidity for the five validation locations during the period 31 July 1999 to 3 August 1999. In general, all simulations represent the observed diurnal cycles in temperature and relative humidity.

The timing of maximum temperature is within 2 h of the observations for both simulations. The amplitude of the diurnal cycle is better captured by LEAF-2 in the first day and by TEB in the subsequent days, with the exception of the S. M. Paulista station (number 5 in Fig. 1b) where LEAF-2 has the best performance during all periods. The maximum differences are less than 2°C for TEB and 3°C for LEAF-2, where LEAF-2 tends to underestimate the diurnal cycle's amplitude.

The simulations perform poorly for the phase and amplitude of minimum temperature, where the greatest discrepancy occurs in the first 13 h of simulation. However, TEB performs slightly better than LEAF-2 during this period and throughout the entire simulation.

In general, the phase and ranges of relative humidity are well simulated. Particularly during the second day of the integrations, TEB outperforms LEAF-2 in the minima of relative humidity. In terms of phase, TEB performs favourably, while observations are lagged about 4 h from LEAF-2. The worst results are found during the third day of simulation when simulated values differ considerably from the observations. The phase of relative humidity maxima is not simulated well by either experiment.

The statistical parameters presented in the last section are now used to evaluate the skill of the simulations. Following Pielke (2002), a simulation has *skill* if the following conditions are met: (1) $\sigma_{sim} \cong \sigma_{obs}$; (2) RMSE $< \sigma_{obs}$; (3) $\text{RMSE}_{UB} < \sigma_{obs}$, where σ_{obs} is the standard deviation of observations and σ_{sim} is the standard deviation of simulations. The results are presented in Tables 4 and 5.

With the exception of Station 1 (IAG-AF), temperature correlation coefficients obtained from LEAF-2 (Table 4) are generally inferior to those obtained from TEB. As one can see from the Tables 4 and 5, since correlation coefficients for temperature are higher than those corresponding to the relative humidity, the simulations appear to have better diurnal phase agreement with observations in temperature. For both simulations' temperatures, the root-mean-square errors are adequately small, with TEB containing errors of less than 1°C.

With the exception of IAG-AF (station number 1 in Fig. 1a), LEAF-2 possesses slightly smaller correlation coefficients in relative humidity than TEB (Table 5). However, for this station, LEAF-2 shows the largest ME and root-mean-square error. This case can be explained by the difference in the soil type of the grid point representative of this area, which is predominantly covered by vegetation (a large park) surrounded by urban areas and is not captured by the vegetation classification in the model grid (not even in the 2-km resolution grid). The root-mean-square error of the simulation with LEAF-2 is slightly larger than the TEB value in most stations, showing that the simulations with TEB are more accurate than the simulations with LEAF-2.

Following the criteria proposed by Pielke (2002), with respect to RMSE and to RMSE_{UB}, only the São Caetano do Sul station (number 4 in Fig. 1a) presents values larger than the standard deviation of observed relative humidity. This same station also shows the lowest correlation coefficients. The comparison between the standard

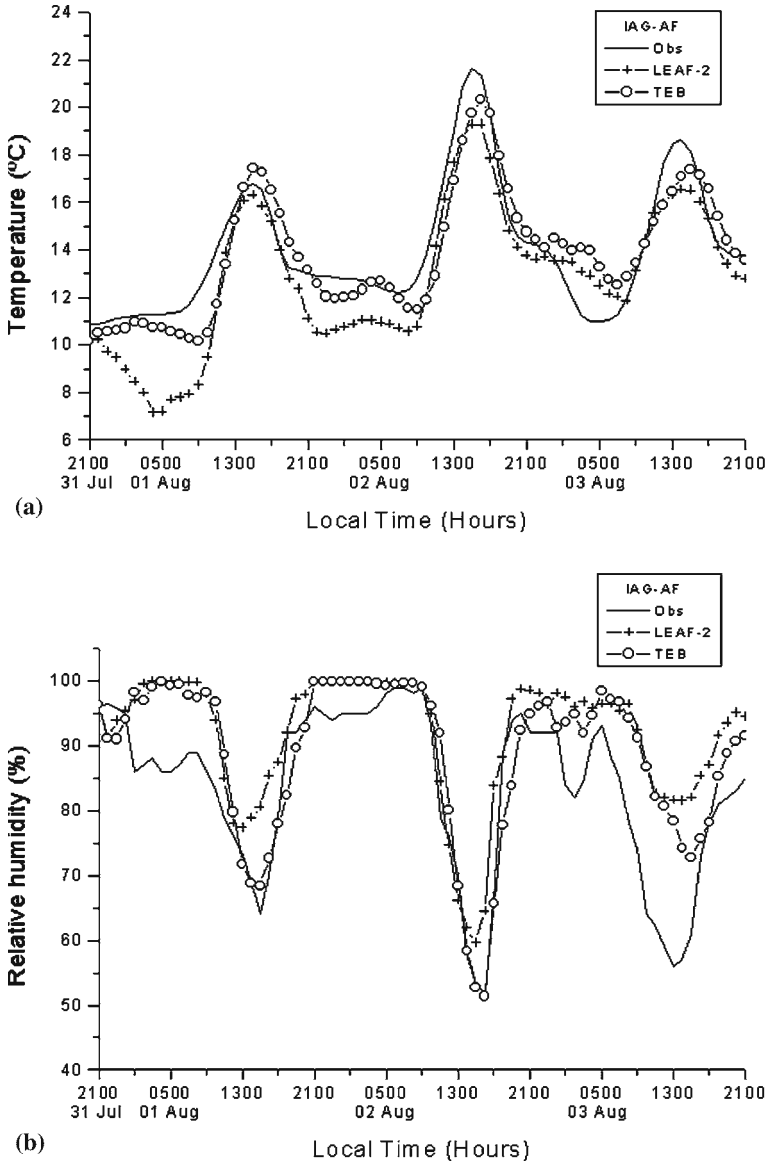

Fig. 2 Comparison between station data and two simulations with RAMS for temperature (top) and relative humidity (bottom) for the station IAG-AF. Simulation 1 was made using LEAF-2 (cross—dashed lines) and simulation 2 was made using TEB (open circles—dashed lines). Simulations were performed in the period from 2100 LT July 31 1999 to 2100 LT, August 3 1999

deviations of simulations and observations compromise the skill. However, based on the other statistical parameters, the 72-h-period relative humidity skill is satisfactory. The results show that TEB is slightly superior to LEAF-2 in terms of both accuracy and precision.

Figure 7 shows vertical wind profiles for 2 August 1999 for the Doppler sodar (Fig. 7a) and the TEB-based simulation (Fig. 7b). Qualitatively, wind direction is in

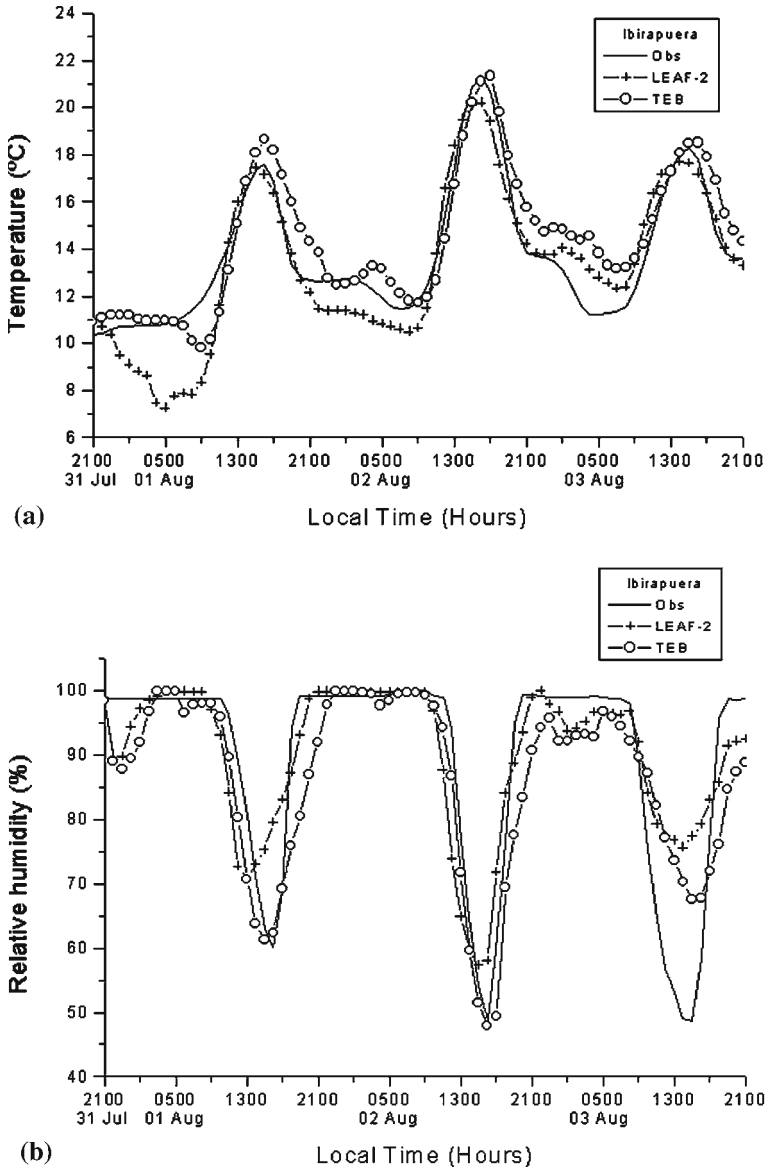

Fig. 3 Same as in Fig. 2 but for the station Ibirapuera

favourable agreement between the observations and model. The largest differences are experienced prior to the sea breeze's arrival at the sodar location (1700–1900 LT). The sodar profile shows south-west winds from the surface to the 500 m level, probably associated with sea-breeze convergence (Fig. 7a). However, this feature is absent in the model (Fig. 7b). In terms of wind speed, the model tends to consistently overestimate the magnitude, although it has been observed that sodar tends to underestimate the wind speed when the magnitude is lower than $3\,\mathrm{m\,s^{-1}}$. The arrival of the sea breeze is well represented by the model (indicated by south-east winds) and occurs by 1800 LT.

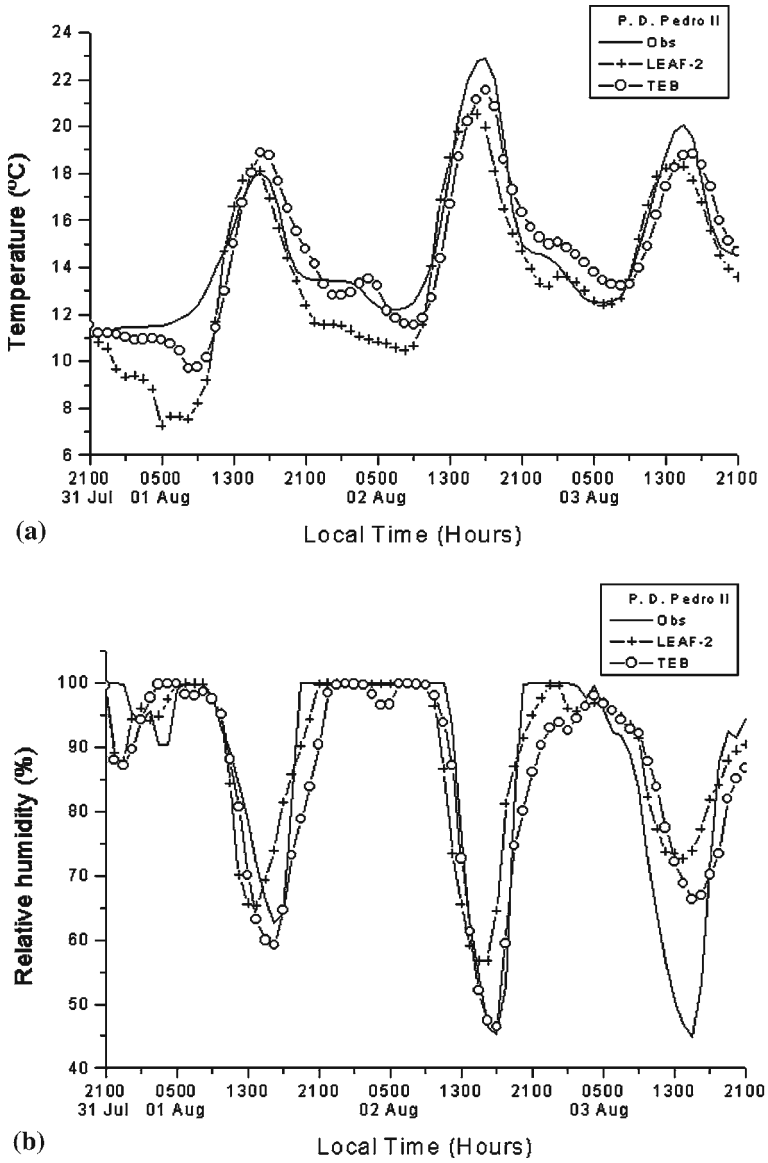

Fig. 4 Same as in Fig. 2 but for the station Pq. D. Pedro II

Figure 8 shows vertical wind profiles between 0300 LT 3 August 1999 and 0300 LT 4 August 1999. Similar to the previous day, the wind direction is well represented by the model. Contrary to the previous day, large-scale weak south-east winds now dominate the flow. The south-east flow quickens the sea-breeze-front propagation contributing to its earlier arrival in the MASP (approximately 1400 LT). These features have great impact on pollution dispersion in MASP due to the increase in turbulence and ventilation.

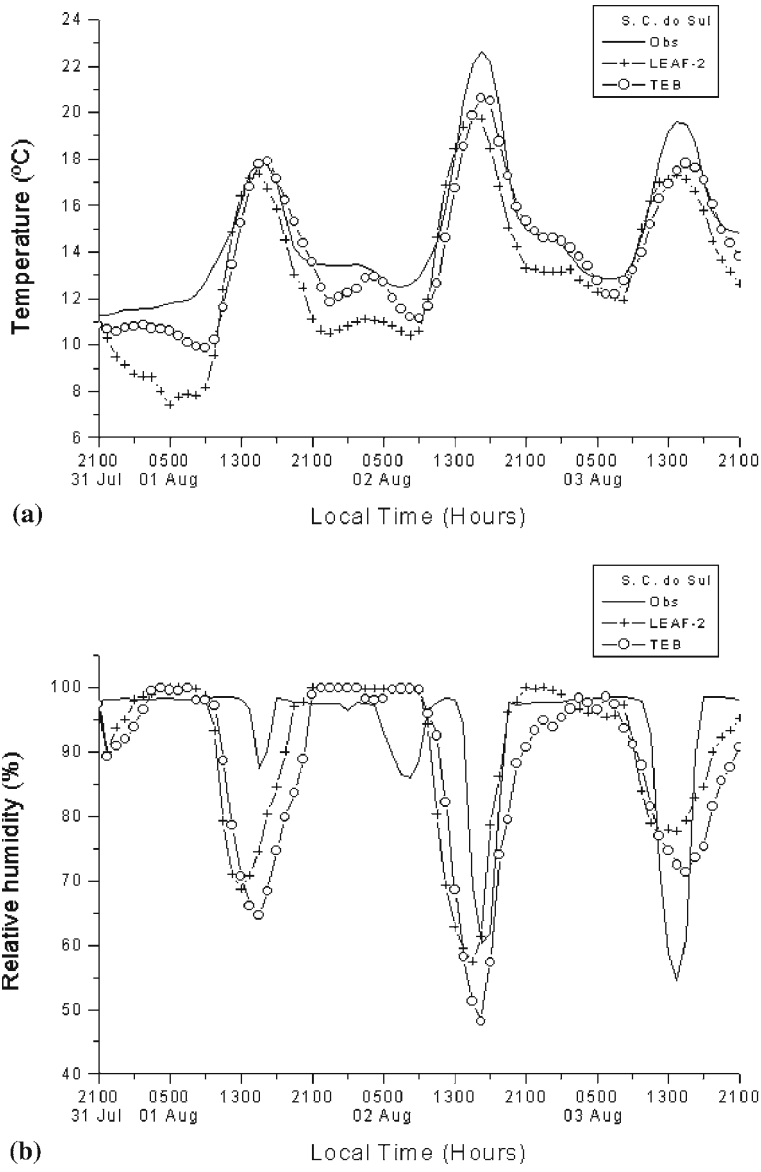

Fig. 5 Same as in Fig. 2 but for the station São Caetano do Sul

4.2 Results from the interaction between the HIC and sea breeze

The simulations with no topography described in Section 3.2 are analysed to identify the interaction between the HIC and sea breeze. During the first few nocturnal hours of the simulations, north-west winds associated with the land breeze are observed. Figure 9 shows vertical profiles of the sea-breeze wind at 0600 LT for the simulation with the city (hereafter, WC) and the simulation without the city (hereafter, NC). At this time, in WC (Fig. 9a) there is a second circulation near the urban region (as

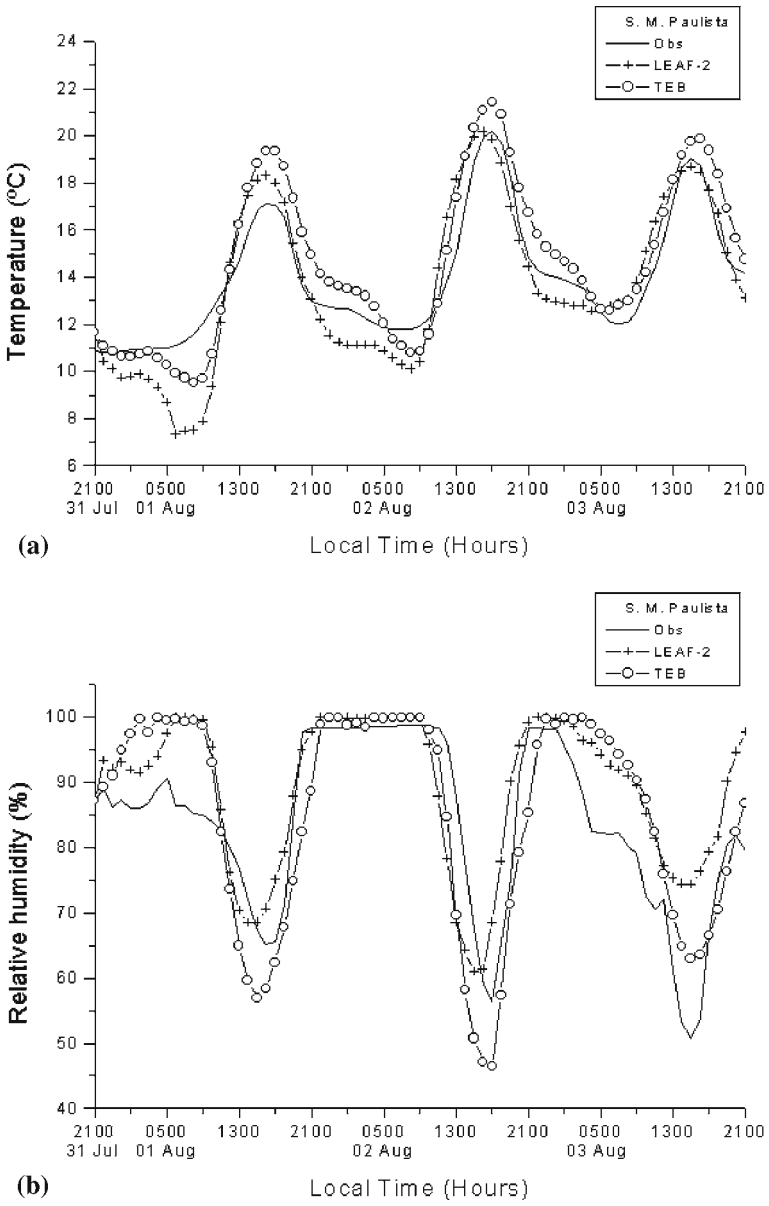

Fig. 6 Same as in Fig. 2 but for the station São Miguel Paulista

denoted by the black bar at the bottom of the figure). This circulation is presumably driven by the UHI. In this region there is a convergence of winds in the south-east portion of the urban area with upward motion extending up to 600 m vertically, which eventually can cause a re-circulation of the air over MASP.

The HIC disappears 8 h into the simulation (i.e. 1000 LT) and by 1100 LT, the sea-breeze circulation emerges (Fig. 10). As the sea breeze develops, the land-breeze cell resides between MASP and the coast, and its depth is similar in both simulations.

Table 4 Skill analyses for temperature

Simulations	R	RMSE	ME	RMSE_{UB}	σ_{sim}	σ_{obs}
Station 1 IAG-AF						
LEAF-2	0.889	1.831	–1.225	1.360	2.993	2.716
TEB	0.888	1.265	–0.193	1.250	2.577	2.716
Station 2 Ibirapuera						
LEAF-2	0.915	1.415	–0.445	1.343	3.300	2.800
TEB	0.919	1.300	0.636	1.134	2.873	2.800
Station 3 Pq. D. Pedro II						
LEAF-2	0.921	1.804	–1.203	1.344	3.455	3.052
TEB	0.928	1.167	–0.220	1.146	3.004	3.052
Station 4 São Caetano do Sul						
LEAF-2	0.924	2.153	–1.764	1.234	3.227	2.815
TEB	0.945	1.244	–0.837	0.921	2.787	2.815
Station 5 São Miguel Paulista						
LEAF-2	0.918	1.534	–0.353	1.493	3.469	2.572
TEB	0.962	1.305	0.681	1.113	3.350	2.572

Table 5 Skill analyses for relative humidity

Simulations	R	RMSE	ME	RMSE_{UB}	σ_{sim}	σ_{obs}
Station 1 IAG-AF						
LEAF-2	0.844	10.807	8.324	6.891	9.849	12.821
TEB	0.831	9.030	5.400	7.237	12.126	12.821
Station 2 Ibirapuera						
LEAF-2	0.833	9.242	0.557	9.225	11.474	16.332
TEB	0.856	8.880	−2.944	8.378	13.776	16.332
Station 3 Pq. D. Pedro II						
LEAF-2	0.844	9.750	1.524	9.631	12.465	17.541
TEB	0.859	9.018	−1.238	8.932	14.557	17.541
Station 4 São Caetano do Sul						
LEAF-2	0.476	11.810	−2.885	11.452	11.688	10.789
TEB	0.585	12.373	−5.576	11.046	13.169	10.789
Station 5 São Miguel Paulista						
LEAF-2	0.792	9.606	5.204	8.074	11.522	13.214
TEB	0.811	9.420	1.380	9.319	16.053	13.214

The direct current has a depth of approximately 600 m with north-west winds up to $0.7\,\text{m}\,\text{s}^{-1}$ and the return flow has a depth of approximately 800 m with south-east winds up to $0.6\,\text{m}\,\text{s}^{-1}$. Updrafts at the sea-breeze front are observed from the surface to about 1000 m. Due to the convergence induced from the UHI, WC contains stronger north-west winds than those in NC over the north-west region of MASP, as one can see in Fig. 10 (regions on the left of the black area in the figures). It is important to note the difference between scales in the bottom of the figures.

Figure 11(a–l) shows the time evolution of the sea breeze for both simulations. As in Fig. 10, there are differences between vector scales in the bottom of the figures. At 1500 LT, there are south-east surface winds from the coast to the city centre in WC.

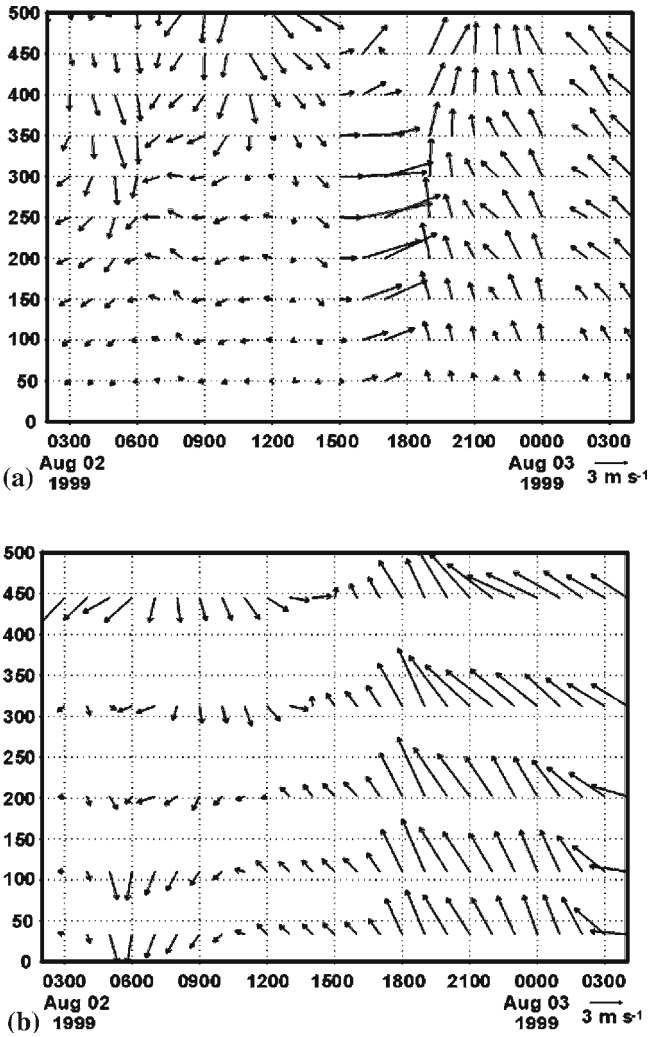

Fig. 7 Wind profiles for the period between 0300 LT August 02, 1999, and 0300 LT August 03, 1999, at the point of latitude 23.559° S and longitude 46.732° W (IAG-USP). In (**a**), obtained by the Doppler sodar. In (**b**), obtained by numerical modelling

Meanwhile, north-west winds are observed in the opposite side of the MASP due to the strong convergence in the centre of the city. The sea-breeze front in WC is located approximately at 46.4° W. In NC, north-west winds retard the advancement of the sea breeze between the urban centre and the coast, with the sea-breeze front located south-east of 46.35° W. The intensity of the winds in the sea-breeze cell is similar in both cases.

At 1600 LT, in the WC simulation, there are relatively intense updrafts in the north-west portion of MASP and in the region of the sea-breeze front, which is located at approximately 46.5° W. The region of north-west winds remains between the urban area and the sea-breeze front in the simulation NC, and the sea-breeze front is located at approximately 46.35° W in this case.

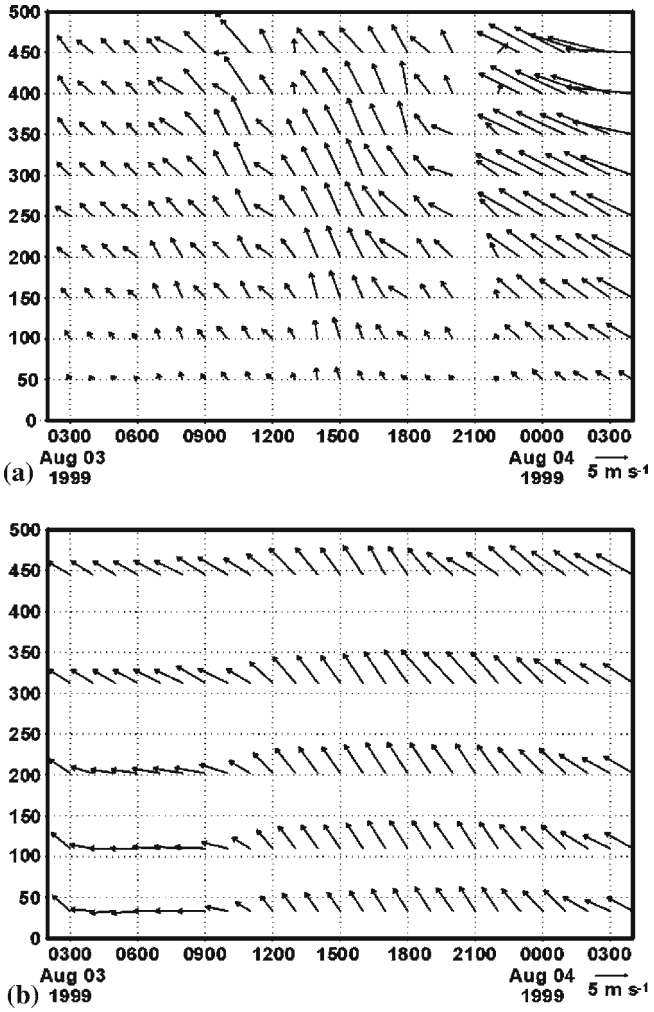

Fig. 8 Same as in Fig. 7 but for the period between 0300 LT August 03, 1999 and 0300 LT August 04, 1999

The HIC is very well defined at 1700 LT, and, in the simulation WC, the sea-breeze cell has its front located at approximately 46.52° W, and it has a vertical extent of approximately 1800 m. In the direct current south-east winds have speeds of up to 4.0 m s^{-1} and in the return flow north-west wind speeds are more than 2 m s^{-1}. In the simulation NC the vertical extension of the sea-breeze cell is similar to that observed in the simulation WC. The region of north-west winds that was located between the sea-breeze front and the urban region at 1600 LT disappears, with the sea-breeze front located at approximately 46.45° W.

In the WC simulation, the sea breeze arrives in the centre of MASP between 1700 LT and 1800 LT, and the updraft located at the centre of the city has speeds up to 0.3 m s^{-1}, from the surface up to 1600 m. In this case, the mean speed of the sea-breeze front is about 2.5 m s^{-1}. At the same time, the NC sea-breeze front is located

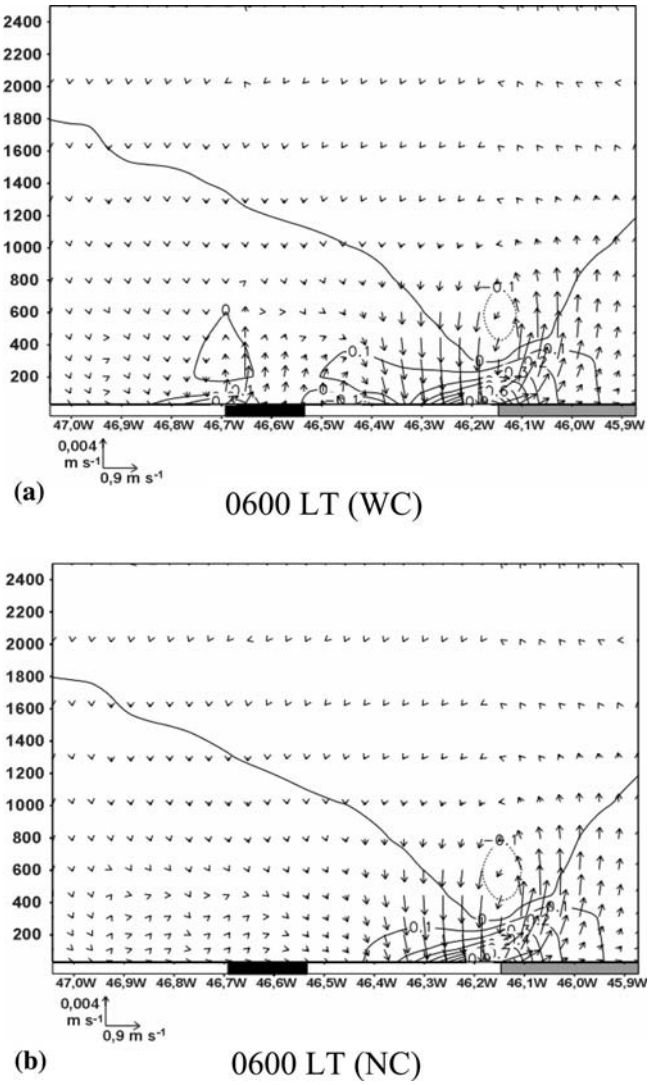

Fig. 9 Vertical profiles of the sea-breeze wind, U_{sb} (m s^{-1}), for the simulations with (WC) and without the city (NC) at 0600 LT. The bar in the bottom of the pictures indicates regions of ocean (dark grey), urban (black) and any type of vegetation (white). Vectors correspond to the composition between vertical (w) and sea-breeze wind (U_{sb}). The intensity of these two components is presented in the bottom left corner of each figure. Contours represent the magnitude of U_{sb} (in m s^{-1})

at 46.52° W. The updrafts in NC (0.09 m s^{-1}) are weaker than those in WC, and the winds in the sea-breeze cell are also weaker varying between 4.5 m s^{-1} in the direct current and 2 m s^{-1} in the return flow.

Up to 2000 LT, the sea-breeze front stalls over MASP in WC, and there is an intensification of the updraft (1900 LT), which has vertical wind speeds of 0.4 m s^{-1}. In NC, the front reaches the centre of MASP at approximately 1900 LT, which is two hours later than WC. The NC front's speed is 2.18 m s^{-1}, and the updraft associated with

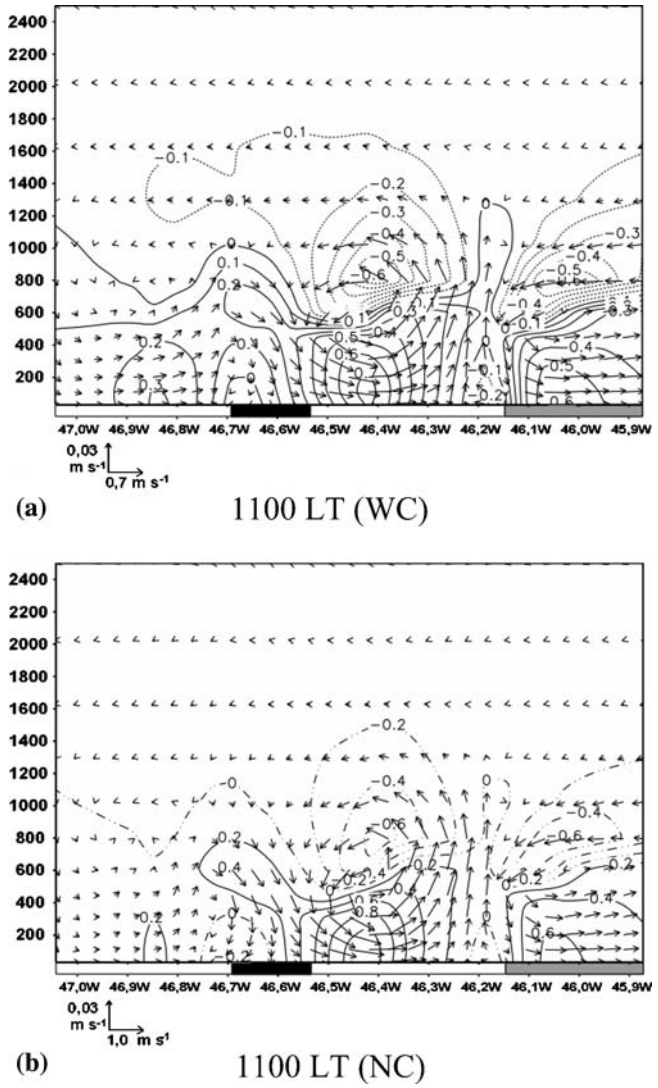

Fig. 10 Same as in Fig. 9 but for 1100 LT

the sea-breeze front has speeds up to 0.09 m s^{-1}. The direct current has wind speeds of 5 m s^{-1} and the return flow wind speeds of about 2 m s^{-1}. The sea-breeze cell has a vertical extension slightly smaller than the one in the case of the simulation WC.

The sea breeze continues beyond MASP in WC between the hours of 2100 LT and 2200 LT. During this period, the sea-breeze front in NC experiences faster propagation, and is due to the fact that, in the WC simulation, the circulation generated by the UHI induces north-west winds downwind of the sea-breeze front, preventing the sea-breeze passage across the urban area. In the case of the NC simulation, this barrier does not exist, allowing a faster propagation of the sea-breeze front.

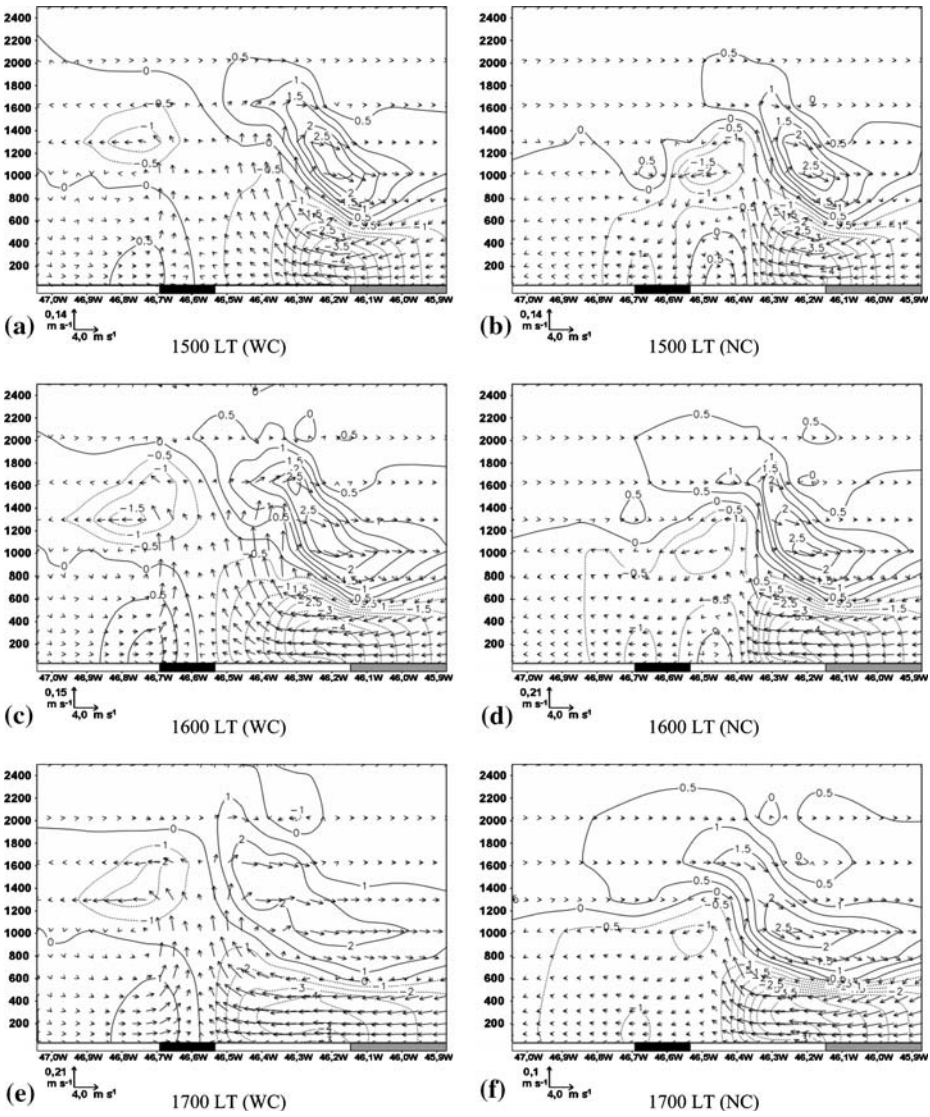

Fig. 11 Time evolution of the sea-breeze front for simulations with (WC) and without city (NC). The bar in the bottom of the pictures indicates regions of ocean (dark grey), urban (black) and any type of vegetation (white). Vectors correspond to the composition between vertical (w) and sea-breeze wind (U_{sb}). The intensity of these two components is presented in the bottom left corner of each figure. Contours represent the magnitude of U_{sb} (in $m\,s^{-1}$)

The faster propagation of the sea breeze in WC before the sea-breeze arrival at MASP is due to the more intense horizontal pressure gradient that exists between this region and the coast, as a consequence of the coupling between the pressure gradient generated by the UHI and the pressure gradient associated with the sea-breeze front. As the UHI develops, a decrease in air density occurs causing ascending movement and a drop of surface pressure, as one can see in Fig. 12a, creating a circular pressure

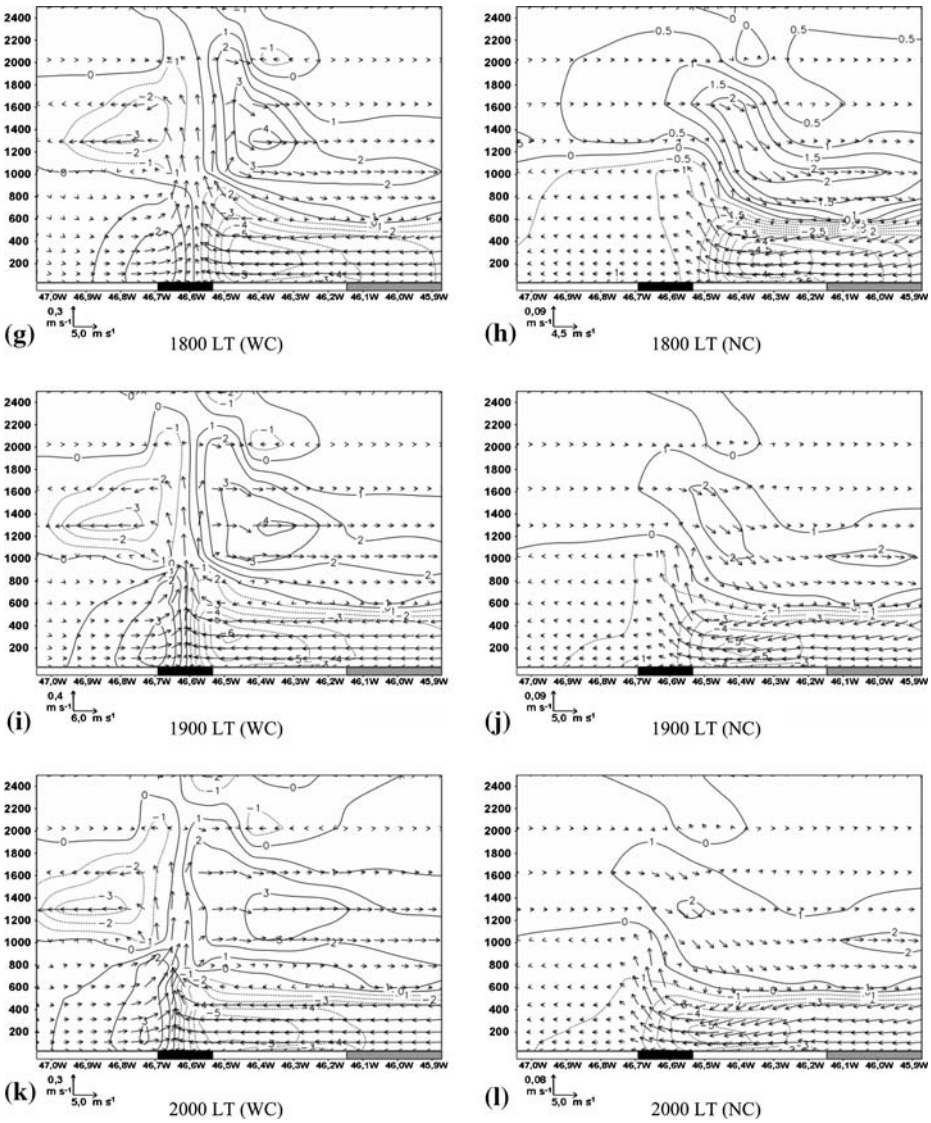

Fig. 11 continued

gradient pattern around the city. This pattern causes acceleration of the order of $0.001\,\mathrm{m\,s^{-2}}$ that increases the sea-breeze front propagation speed. At the same time, these features are not observed in NC (Fig. 12b). In NC the pressure gradient is more likely to be perpendicular to the coastline, following the sea-breeze front. At 1700 LT (Fig. 12c, d) this circular pattern in the pressure field remains in the WC simulation preventing the advance of the sea-breeze front, as mentioned before, due to the opposite acceleration on the sea-breeze cell in the northern portion of MASP. In the NC simulation, there is no acceleration counteracting the sea-breeze front propagation. At 2100 LT (Fig. 12 e, f), after the UHI effects disappear, the sea breeze

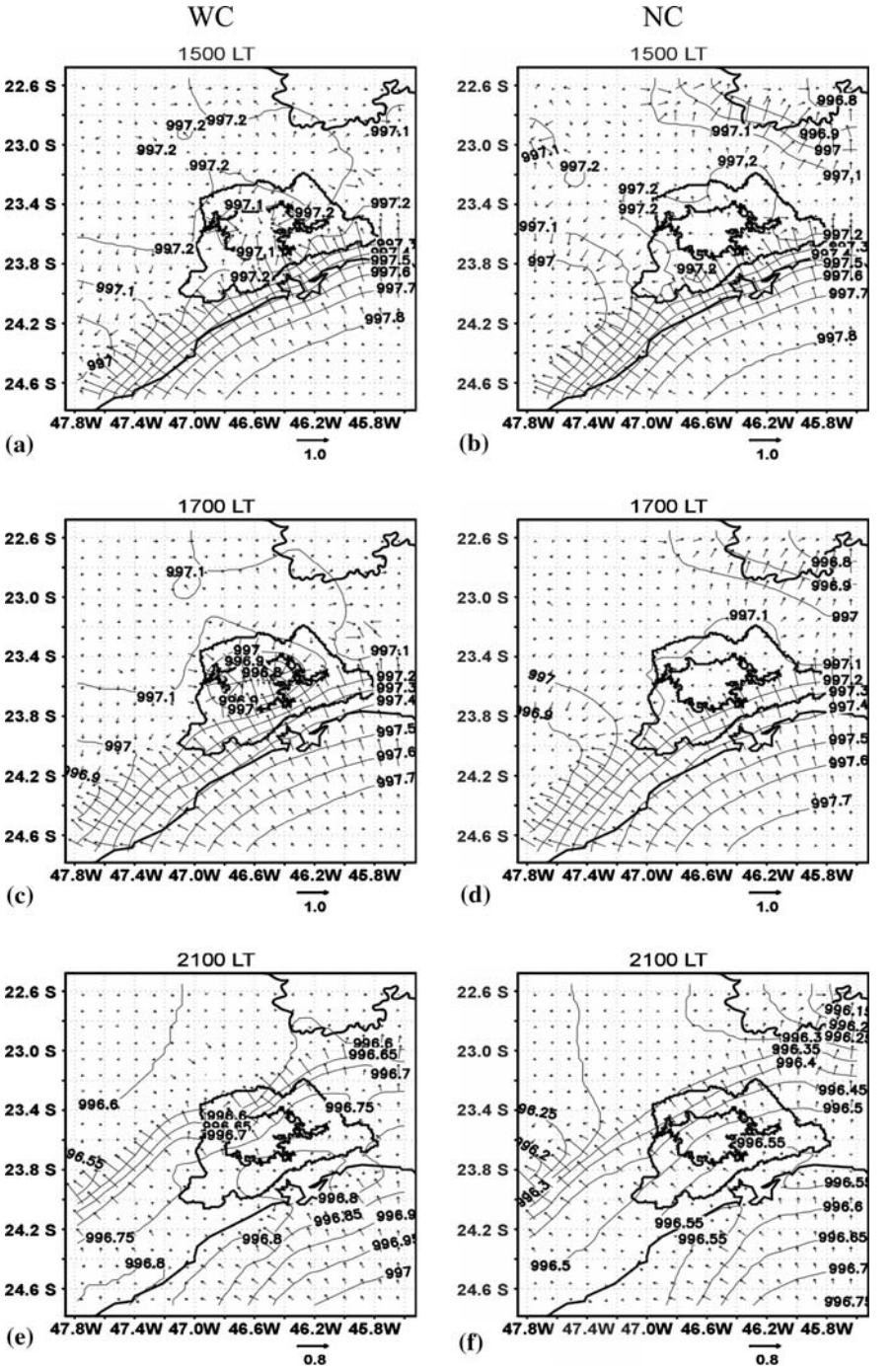

Fig. 12 Contours of surface pressure (h Pa) for WC (left and NC right) and vectors of horizontal acceleration due to the pressure gradient force (10^{-3} m s^{-2}). Contours in the figures show the political limits of MASP and its most urbanised area. In (**a**) and (**b**) for 1500 LT, (**c**) and (**d**) for 1700 LT and (**e**) and (**f**) for 2100 LT

in WC simulation continues its propagation inland and the pattern is similar to the one observed in NC simulation.

It is interesting to note that horizontal pressure gradients in the north-east and south-west corners of the domain in the NC case after 1500 LT (Fig. 12b, d, f) are associated with precipitation triggered by the propagating sea-breeze front. In the WC case, precipitation is concentrated over the city due to the stronger thermal contrast that leads to the convergence over the city and larger updraft intensities. The presence of the urban region contributes to vertical velocities approximately five times stronger than would be the case if the city did not exist. These updrafts contribute considerably to the vertical transport of humidity (not displayed). It was observed during the WC simulations that this transport of humidity could reach heights of up to 2000 m. The same feature is not observed in the NC simulation.

5 Conclusions

A detailed urban parameterisation coupled with RAMS is used to study two important local circulations in MASP: the UHI and the sea breeze. It is found that the TEB scheme has the ability to represent the particular features of urban regions, especially during a period of 48 h, better than schemes that are usually used in operational numerical weather prediction models. Correlation coefficients for observed and modelled temperatures were found to be at least 0.9. For relative humidity the correlation coefficients were slightly lower at about 0.85.

The interactions between the urban HICs and the sea breeze were explored using sensitivity tests. Initially, the UHI acts to accelerate the sea-breeze front into the MASP until it reaches the centre of the urban region. This is in agreement with the results from Khan and Simpsom (2001). The presence of the urban region increases the sea-breeze-front propagation speed by about $0.32\,\mathrm{m\,s^{-1}}$ when compared with the situation where no city exists. Additionally, due to the strong convergence zone in the centre of the city the circulations induced from MASP act to stall the sea breeze over the city for about two hours, carrying a large amount of humidity from the surface to upper levels of the urban atmosphere. These results agree with those from Yoshikado (1994) and Ohashi and Kida (2002). The UHC also contributes to increased wind speed in the sea-breeze circulation cell. The prevention of sea-breeze-front propagation continues until the UHI effect disappears.

Acknowledgements The authors would like to thank the Fundação de Amparo à Pesquisa do Estado de São Paulo (FAPESP) and the Colorado State University (CSU) for the financial support to this research. We also acknowledge Valery Masson (Centre National de Rescherches Météorologiques) and METEO-FRANCE for use of the Town Energy Budget model and the anonymous reviewers for their clarifying comments. William Cotton acknowledges NSF ATM-0327652 for supporting his contributions to the research.

References

Ado HY (1992) Numerical study of the daytime urban effect and its interaction with the sea-breeze. J Appl Meteorol 31:1146–1164

Baik JJ, Kim YH, Chun HY (2001) Dry and moist convection forced by an urban heat island. J Appl Meteorol 40(8):1462–1475

Baik JJ, Kim JJ (2002) On the escape of pollutants from urban street canyons. Atmos Environ 36:527–536

Balling RC, Skindlov JA, Philips DH (1990) The impact of increasing summer mean temperatures on extreme maximum and minimum temperatures in Phoenix, Arizona. J Climate 3:1491–1494
Bornstein RD (1975) The two-dimensional URBMET urban boundary layer model. J Appl Meteorol 14:1459–1477
Changnon SA, Huff FA, Semonin RG (1971) METROMEX: an investigation of inadvertent weather modification. Bull Amer Meteorol Soc 52:958–968
Cotton WR et al (2003) RAMS 2001: current status and future directions. Meteorol Atmos Phys 82:5–29
Dixon PG, Mote T (2003) Patterns and causes of Atlanta's urban heat island – initiated precipitation. J Appl Meteorol 2:1273–1284
Gedzelman SD, Austin S, Cermak R, Stefano N, Partridge S, Quesenberry S, Robinson DA (2003) Mesoscale aspects of the urban heat island around New York City. Theor Appl Climatol 75:29–42
Grimmond CSB, Oke TR (1999) Aerodynamic properties of urban areas derived from analysis of surface form. J Appl Meteorol 38:1262–1292
Hill GE (1974) Factors controlling the size and spacing of cumulus clouds as revealed by numerical experiments. J Atmos Sci 31:646–673
Khan SM, Simpson RW (2001) Effect of a heat island on the meteorology of complex urban airshed. Boundary-Layer Meteorol 100:487–506
Kimura R (1976) Effects of general flows on a heat island convection, part 1 – linear theory for the uniform flow. J Meteorol Soc Japan 54:308 –320
Kim YH, Baik JJ (2002) Maximum urban heat island intensity in Seoul. J Appl Meteorol 41:651–659
Kim JJ, Baik JJ (2004) A numerical study of the effects of ambient wind direction on flow and dispersion in urban street canyons using the RNG k–e turbulence model. Atmos Environ 38:3039–3048
Klemp JB, Wilhelmson RB (1978) The simulation of three-dimensional convective storm dynamics. J Atmos Sci 35:1070–1096
Lilly DK (1962) On the numerical simulation of buoyant convection. Tellus, XIV 2:148–172
Mahrer Y, Pielke RA (1977) A numerical study of the airflow over irregular terrain. Beit Phys der Atmos 50:98–113
Masson V (2000) A physically-based scheme for the urban energy budget in atmospheric models. Boundary-Layer Meteorol 94:357–397
Morris CJG, Simmonds I, Plummer N (2001) Quantification of the influences of wind and cloud on the nocturnal urban heat island of a large city. J Appl Meteorol 40:169–182
Ohashi Y, Kida H (2002) Local circulations developed in the vicinity of both coastal and inland urban areas: a numerical study with a mesoscale atmospheric model. J Appl Meteorol 41:30–45
Oke TR (1978) Boundary layer climates, 2nd edn. Rutledge, London and New York, 435 pp
Pielke RA et al (1992) A comprehensive meteorological modeling system – RAMS. Meteorol Atmos Phys 49:69–91
Pielke RA Sr (2002) Mesoscale meteorological modeling, 2nd edn. Academic Press, San Diego, 676 pp
Rozoff CM, Cotton WR, Adegoke JO (2003) Simulation of St. Louis, Missouri, land use impacts on thunderstorms. J Appl Meteorol 42(6):716–738
Sailor DJ (1995) Simulated urban climate response to modifications in surface Albedo and vegetative cover. J Appl Meteorol 34:1694–1704
Smagorinsky J (1963) General circulation experiments with the primitive equations: 1. the basic experiment. Mon Wea Rev 91:99–164
Stull RB (1988) An introduction to boundary layer meteorology. Kluwer Academic Publishers, The Netherlands, 670 pp
Tarifa JR, Azevedo TR 2001, Os climas na cidade de São Paulo: teoria e prática. GEOUSP – Coleção Novos Caminhos, 4, São Paulo, 199 pp
Walko RL et al (2000) Coupled atmosphere-biophysics-hydrology models for environmental modeling. J Appl Meteorol 39:931–944
Wieringa J (1993) Representative roughness parameters for homogeneous terrain. Boundary-Layer Meteorol 63:323–363
Wilks DS (1995) Statistical methods in the atmospheric sciences. Academic Press, San Diego, 467 pp
Yoshikado H (1994) Interaction of the sea-breeze with urban heat islands of different sizes and locations. J Meteorol Soc Japan 72:139–143
Yoshikado H, Tsuchida M (1996) High levels of winter air pollution under the influence of the urban heat island along the shore of Tokyo Bay. J Appl Meteorol 35:1804–1814